Chemical Science

ROYAL SOCIETY OF CHEMISTRY

EDGE ARTICLE

View Article Online
View Journal

Cite this: DOI: 10.1039/d6sc01451h

All publication charges for this article have been paid for by the Royal Society of Chemistry

Site-specific post-translational modification detection by polar charged engineered MspA nanopores

Shijun Lin,[a] Yakun Yi,[b] Yiheng Liu,[a] Minglun Li,[c] Fan Xia,*[a] Hai-Chen Wu*[b] and Xiaoding Lou*[a]

Deciphering the complex chemical code of post-translational modifications (PTMs) is fundamental to proteomics but remains challenging due to the low abundance of modified proteins and the difficulty in resolving isobaric positional isomers. Conventional mass spectrometry and affinity-based methods often lack the sensitivity or specificity required to capture this full chemical diversity. Here, we present a general strategy for site-specific PTM recognition based on MspA nanopores engineered with polar charged residues. By systematically tuning the constriction site (position N91) with polar charged residues, we introduced specific electrostatic, electroosmotic flow and steric interactions that dramatically enhance molecular recognition capabilities. This engineered interface enabled the label-free discrimination of 10 distinct PTM types across 26 peptides, including phosphorylation, glycosylation, and—reported here for the first time *via* nanopore sensing—lysine crotonylation and succinylation. Furthermore, the nanopore is capable of distinguishing subtle positional isomers. Coupled with a machine learning algorithm that classifies single-molecule events with >98% accuracy, our findings establish a generalizable principle of electrostatic gating for PTM profiling, offering a versatile chemical tool for next-generation single-molecule proteomics.

Received 19th February 2026
Accepted 8th May 2026

DOI: 10.1039/d6sc01451h

rsc.li/chemical-science

Introduction

Post-translational modifications (PTMs) constitute the complex "chemical code" that exponentially expands the functional diversity of the proteome.[1–3] PTMs modulate protein conformation,[4] stability,[5] interaction networks,[6] and subcellular localization,[7] and are critical regulators of signaling,[8] development,[9] and disease.[10] Therefore, accurate characterization of PTM patterns and modification sites is essential for understanding biological pathways and for identifying diagnostic and therapeutic targets.[11,12] Conventional analytical methods such as mass spectrometry (MS) and immunoassays have achieved considerable success in PTM profiling.[13–15] However, MS-based techniques are typically limited by insufficient sensitivity for low-abundance modifications, overlapping mass spectra of isobaric groups, and complex sample preparation procedures.[16,17] Antibody-based techniques, though sensitive, are limited by the availability and specificity of antibodies and are often restricted to one PTM type per assay.[18,19] Therefore, developing a label-free, single-molecule strategy capable of deciphering this chemical complexity remains an urgent challenge in chemical biology.

Nanopore sensing, which directly detects single molecules as they translocate through a nanoscale pore,[20–22] offers unique advantages for PTM analysis.[23–26] Nanopore sensing can operate label-free and amplification-free, allowing real-time detection of individual peptides with sub-nanometer resolution.[27–29] However, designing nanopores capable of distinguishing a broad spectrum of PTMs with high specificity remains a challenge. Previous studies have relied on engineering approaches, with limited scope across PTM types. To address this gap, we sought to develop a general strategy for PTM detection by systematically tuning nanopore–analyte interactions. Since most PTMs occur on polar amino acid residues (*e.g.*, lysine, arginine, serine), and often involve changes in charge, polarity, and steric bulk,[30–32] we hypothesized that introducing polar charged residues at the nanopore constriction would enhance sensitivity and broaden detection capabilities.

MspA, a robust octameric nanopore from *Mycobacterium smegmatis*, has previously demonstrated utility in DNA sequencing and peptide analysis.[33–35] Its constriction site, centered around residue N91, was selected for engineering due to its critical role in analyte sensing. In this study, we executed

[a]State Key Laboratory of Geomicrobiology and Environmental Changes, Faculty of Materials Science and Chemistry, China University of Geosciences, Wuhan 430074, China. E-mail: louxiaoding@cug.edu.cn; xiafan@cug.edu.cn

[b]Beijing National Laboratory for Molecular Sciences, Key Laboratory of Analytical Chemistry for Living Biosystems, Institute of Chemistry, Chinese Academy of Sciences, Beijing 100190, China. E-mail: haichenwu@iccas.ac.cn

[c]State Key Laboratory of Polymer Science and Technology, Changchun Institute of Applied Chemistry, Chinese Academy of Sciences, Changchun 130022, China

a systematic engineering of the MspA constriction site, generating nine variants with diverse polarities to precisely modulate nanopore–analyte interactions. Our investigation revealed that variants incorporating polar charged residues—specifically lysine and glutamate—dramatically enhanced sensing capabilities. These engineered nanopores enabled the label-free identification of 10 distinct PTMs at single modification sites, including tyrosine, threonine, and serine phosphorylation; lysine methylation and acetylation; serine acetylation and glycosylation; threonine glycosylation; and notably, lysine crotonylation and succinylation, both reported here for the first time using nanopore sensing. Multiplexed discrimination of up to nine PTM types was achieved in a single measurement. Furthermore, the system distinguished positional isomers of phosphorylated peptides based on unique ion current features. To facilitate accurate event classification, a machine learning model was developed, achieving over 98% validation accuracy. These results highlight the essential role of polar charged residues at the nanopore constriction for enhancing PTM recognition. Our work presents a generalizable and scalable strategy for single-molecule PTM detection, providing a versatile platform for advancing nanopore-based proteomic technologies.

Results and discussion

Detection and discrimination of diverse PTMs with engineered MspA nanopores

In this study, we constructed eight single-point mutants of MspA based on the M2 MspA, replacing N91 with glutamine (Q), histidine (H), aspartic acid (D), arginine (R), lysine (K), glutamic acid (E), phenylalanine (F), or tryptophan (W) (Scheme 1 and Fig. S1). These substitutions represent a range of polarity and charges. All mutants were successfully expressed and purified, as confirmed by MALDI-TOF and high performance liquid chromatography (HPLC) analyses (Fig. S2 and S3). Single-channel electrophysiological recordings demonstrated stable open-pore currents across all variants in 1.0 M NaCl, 10.0 mM HEPES, pH 7.4 at +50 mV. The current–voltage (*I–V*) relationships confirmed functional pore formation and revealed subtle differences in conductance among mutants (Fig. 1 and S4–S6). Notably, when examining the negative voltage regime, we observed distinct gating behaviors among the mutants (Fig. S7). Most mutants exhibited voltage-dependent gating starting around −10 mV, whereas MspA-D and MspA-H showed gating only at more negative potentials (approximately −40 mV). In contrast, MspA-F and MspA-W displayed pronounced gating that led to complete pore blockade in the absence of analytes under negative voltages; the open state could be restored only by reversing the voltage polarity. These gating characteristics are consistent with recent reports on M2-MspA.[36] These engineered pores were then tested for their ability to detect 10 chemically distinct PTMs, with clear current blockade events observed across the set.

To systematically evaluate the recognition capabilities of MspA mutant nanopores toward diverse PTMs, we constructed a peptide library in which all peptides shared the same sequence but carried one of eight modification groups: phosphorylation, methylation, acetylation, glycosylation, crotonylation, succinylation, nitration, or sulfonation (Fig. 2a). The corresponding chemical structures are shown in Fig. 2b. Nanopore measurements using engineered MspA mutants revealed that five PTMs—phosphorylation, acetylation, glycosylation, crotonylation, and succinylation—produced distinct current signatures, whereas methylation, nitration, and sulfonation could not be clearly resolved under the tested conditions (Fig. S8–S15). Also, to establish a biologically relevant PTM detection strategy, we engineered KT (Tau175-190) peptide by substituting lysine with glutamine/glutamate (Q/E), mitigating charge interference in MspA nanopores (Fig. S16–S28).

To quantify discrimination performance, we analyzed the relative residual current ($\Delta I/I_0$) values of the PTM peptides across different MspA variants. Mutants bearing polar charged residues, particularly MspA-K and MspA-E, consistently enabled detection across the widest range of PTM peptides, highlighting the essential role of electrostatic interactions and electroosmotic flow (EOF) in PTM detection (Fig. 2c and S29). The electroneutral pores showed no detectable events, indicating that electrophoretic force alone is insufficient to drive peptide translocation under these conditions. However, this does not exclude the possibility of capture under higher voltages or higher sampling rates. In contrast, the high charge density at the constriction sites of MspA-K and MspA-E provides strong ion selectivity and, consequently, generates EOF. This electroosmotic flow offers a significant driving force that actively pulls peptides through the nanopore, enabling analyte capture and detection.

To elucidate the underlying mechanism, we focused on MspA-K and carried out molecular docking simulations with three representative peptides: a phosphorylated peptide (PD-p), a crotonylated peptide (PD-cr), and the corresponding unmodified peptide (PD). Docking models showed that the docking interface revealed that PD-p formed an extensive hydrogen-bonding network—24 hydrogen bonds in total, including nine with the K91 residue—whereas PD-cr and PD formed only 10 and 9 hydrogen bonds, respectively. The denser hydrogen-bonding and electrostatic complementarity in the PD-p–MspA-K complex likely enhance conformational stability, prolong translocation dwell times, and amplify current differences, thereby improving PTM discrimination (Fig. S30–S32).

In practice, MspA-K was able to clearly distinguish all the nine PTM peptide groups with distinct signal distributions (Fig. 2d). To streamline classification and minimize manual bias, we developed a machine learning pipeline. Each signal event was described by four features: relative residual current ($\Delta I/I_0$), dwell time, standard deviation, and instantaneous frequency. We evaluated 30 different models, including decision trees, support vector machines (SVMs), *k*-nearest neighbors (KNN), discriminant analysis, ensemble methods, and neural networks (Table S4). The Bagged Trees ensemble model exhibited the best performance, achieving 98.2% validation accuracy and 98.3% test accuracy (Fig. 2e and S33), enabling robust and automated identification of PTM types from nanopore data.

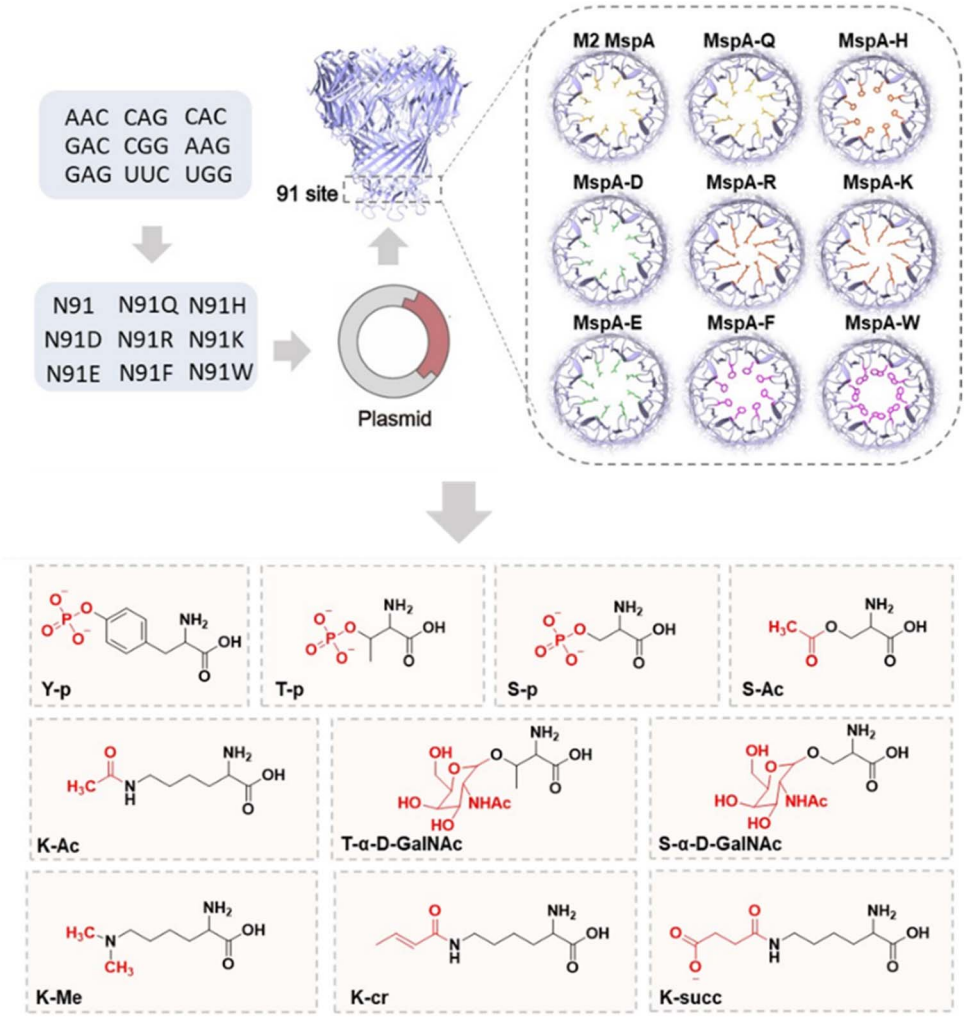

Scheme 1 Single-point mutants of MspA were constructed and enabled the highly specific detection of target post-translational modifications (PTMs).

Detection of phosphorylated peptides

Protein phosphorylation plays a central role in regulating key biological processes such as cellular signaling.[37] Its functional outcomes depend critically on both the specific residue modified and the precise number of phosphorylation events (*i.e.*, phosphorylation stoichiometry).[38] However, conventional techniques face considerable challenges in distinguishing peptides with similar or identical net charges but different phosphorylation sites.[39–41] These limitations primarily arise from the difficulty of detecting variations in ionization efficiencies and interference from complex biological samples.

In this study, we found that polar charged mutants of MspA can recognize a wide variety of PTMs on peptides, underscoring the importance of charge–charge interactions in PTM detection. This recognition is further facilitated by EOF, which enhances the capture and translocation of peptides through the nanopore, thereby contributing to the sensitivity and discriminative capability of the mutants (Fig. S34–S37). To further evaluate their potential, we used MspA-K to discriminate phosphorylated peptides (Fig. 3a). We designed peptide substrates containing none (HY), one (HY-1p), two (HY-2p), or three (HY-3p) phosphoryl groups. With increasing numbers of phosphoryl groups, the current blockade events displayed distinct graded features corresponding to first-, second-, and third-level blockades (Fig. 3b–h). Notably, such phosphorylation-dependent graded signal characteristics have not been previously reported for any nanopore sensor. We also observed a positive correlation between event frequency and peptide concentration (Fig. S38). Together, these findings demonstrate that the MspA-K nanopore can reliably detect phosphorylation modifications through characteristic current blockades, highlighting its promise as a powerful tool for post-translational modification analysis.

To elucidate the mechanism underlying phosphorylated peptide recognition by MspA-K, we performed all-atom molecular dynamics (MD) simulations. In the setup, the phosphorylation sites within the peptide are positioned within the constriction position of MspA-K nanopore, with the Y2, Y8 and Y10 sites. Notably, for our simulations, the peptide was modeled with double phosphorylation at both Y8 and Y10 sites (referred to as Y8@Y10). The Y2 and Y8@Y10 positions of the

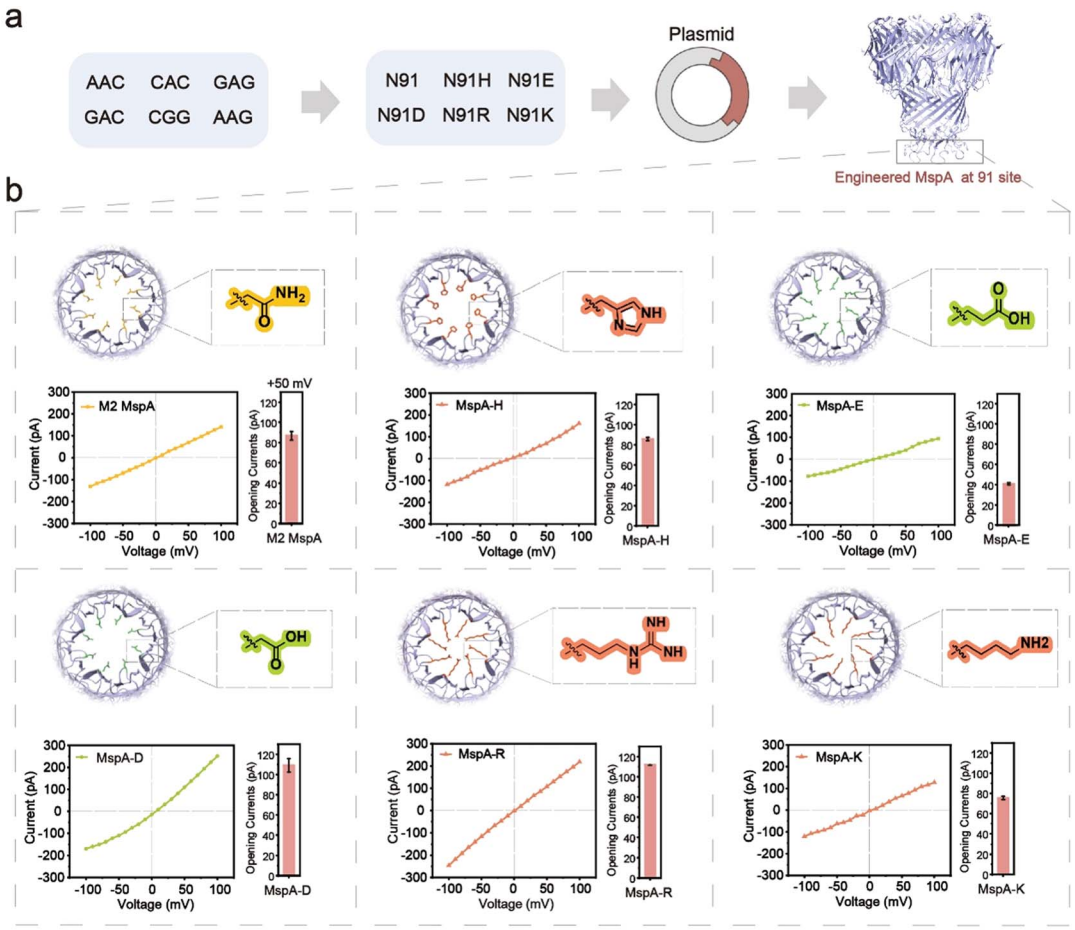

Fig. 1 (a) Schematic of the plasmid construct of MspA mutants. Single-point mutants of MspA were constructed by replacing asparagine at N91 with, histidine (H), glutamic acid (E), aspartic acid (D), arginine (R) and lysine (K). (b) The top view and current–voltage (*I*–*V*) relationships of MspA mutants, including the histogram of the open pore currents (I_0) of MspA mutants at +50 mV. The structure shown in the top view is a homology model based on WT MspA (PDB 1UUN). It is intended to illustrate the location and structure of the mutated residue and does not represent the precise conformation of the mutants. The applied voltage was ramped −100 mV to +100 mV with 10 mV intervals. All data were acquired in the buffer of 1.0 M NaCl, 10 mM HEPES, pH 7.4.

peptides were positioned adjacent to MspA-K (Fig. 4a and S39–S40). The combinations of phosphorylation groups at these sites correspond to HY, HY-1p, HY-2p, or HY-3p, allowing quantitative analysis of the binding free energy ($\Delta G_{binding}$, kcal mol^{-1}) between peptides carrying different numbers of phosphoryl groups and the N91K residue in the constriction zone, along with the ionic currents generated during simulated translocation. The HY peptide was included in simulations as a structural reference to explore potential peptide–pore interactions; while no obvious translocation events were detected for HY experimentally, these simulations offer mechanistic insights into molecular–scale interactions that may occur during peptide–pore encounters. The HY peptide was included in simulations as a structural reference to explore potential peptide–pore interactions; while no obvious translocation events were detected for HY experimentally, these simulations offer mechanistic insights into molecular scale interactions that may occur during peptide–pore encounters. In these simulations, HY, HY-1p, HY-2p, and HY-3p all translocated through the MspA-K nanopore within comparable simulation times. The calculated $\Delta G_{binding}$ exhibited a phosphorylation-dependent enhancement (Fig. 4b), with HY-3p showing the strongest affinity for the nanopore.

Comparison of binding free energies at the two positions further indicated that HY-1p, HY-2p, and HY-3p generate one, two, and three distinct energy barriers, respectively, during translocation (Fig. 4c). These barriers likely account for the experimentally observed graded blockade distributions. The experimentally measured blockade currents (Fig. 4d) showed excellent agreement with the simulated values (Fig. 4e and S41). For the multi-level experimental signals observed in HY-2p and HY-3p, the representative experimental current values plotted in Fig. 4d were determined by extracting the amplitudes of all blockade events and applying a gaussian fit to the resulting distribution. Thus, the plotted experimental values represent the statistically most probable states (weighted average), which are then compared with the simulated current of the predominant binding conformation. Since ionic current is strongly correlated with the effective volume of the nanopore constriction, the markedly reduced residual currents of phosphorylated

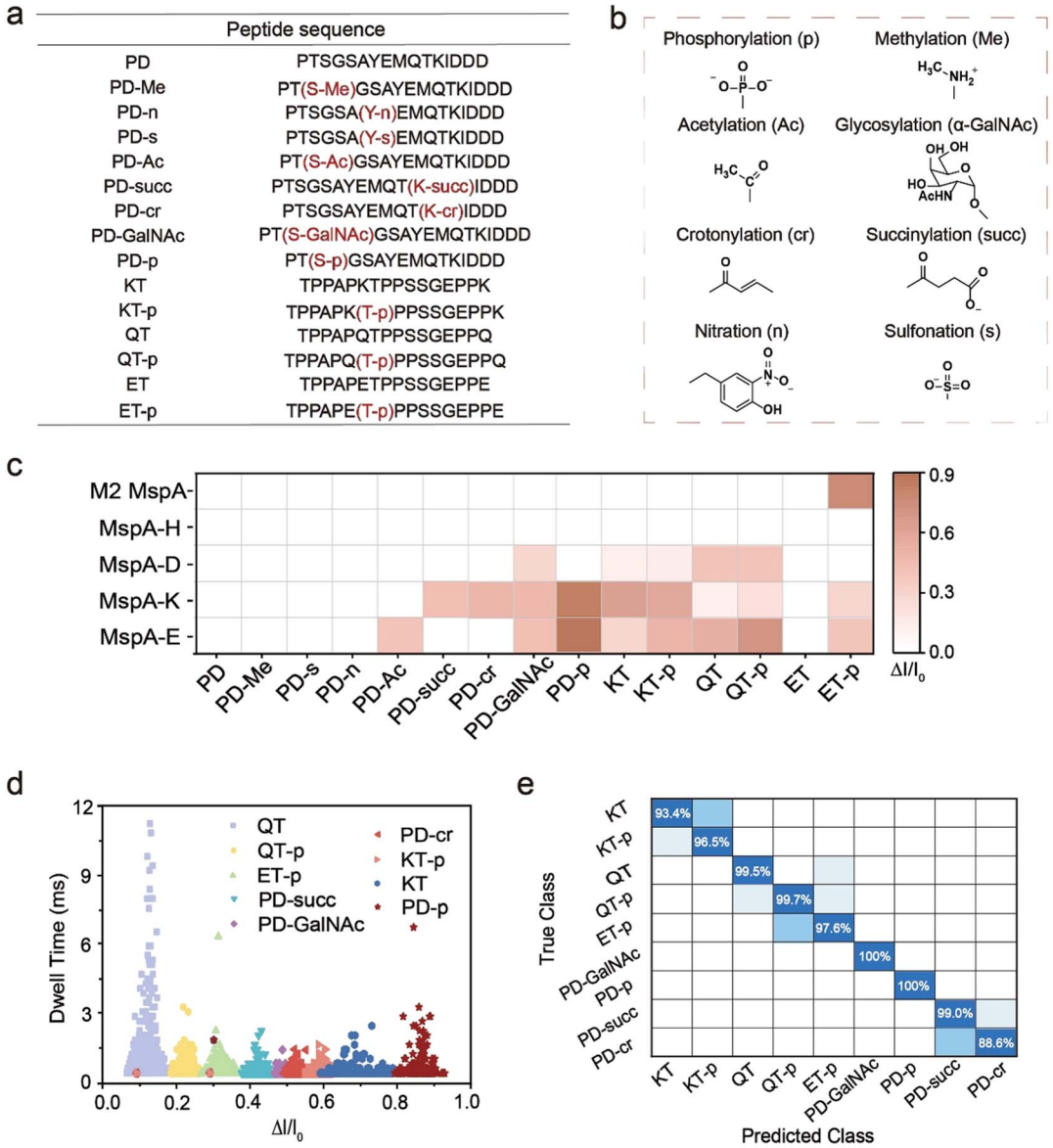

Fig. 2 (a) Schematic of the peptide sequences investigated featuring eight different types of PTM groups. (b) Detailed chemical structures of the PTM groups. (c) The relative residual current ($\Delta I/I_0$) heatmap of MspA mutants for detecting different PTM peptides. All peptides were analyzed at 5.0 μM and the glycosylated peptide at 50.0 μM. (d) The scatter-plot showing the relationship between dwell time and $\Delta I/I_0$ for nine PTM peptide groups across MspA-K nanopore. (e) PTM groups identification by machine learning. The confusion matrix of nine types of PTM groups classification in MspA-K generated using the bagged trees model. The validation accuracy was 98.2%, and the test accuracy was 98.3%. All data were acquired in the buffer of 1.0 M NaCl, 10.0 mM HEPES, pH 7.4.

peptides compared to their unmodified counterparts suggest that the steric bulk of phosphate groups effectively restricts ion flux through the MspA-K channel.

Radial distribution function (RDF) analysis of K91–peptide interaction distances revealed a pronounced probability peak at ~0.9 nm, with the intensity of this peak decreasing progressively with fewer phosphoryl groups (Fig. 4f). To provide a more intuitive comparison of the differences in radial distribution among different peptides, Fig. 4g shows a magnified view of the region presented in Fig. 4f. From this enlarged view, it can be seen more clearly that the difference in the peak radial distribution distance between HY and HY-3p is approximately 0.1 nm. The distribution probability of the center-of-mass displacement (ΔL_z) shown in Fig. 4h (Y2 + MspA-K), further demonstrated that HY exhibits minimal displacement due to its low net charge, which limits effective translocation. In contrast, HY-1p and HY-2p showed larger displacements, corresponding to shorter blockade times. Interestingly, HY-3p exhibited markedly reduced displacement—a seemingly counterintuitive outcome that can be attributed to its high binding free energy with K91, which substantially retards translocation and extends blockade duration. While our current simulations focus primarily on the ionic current blockade caused by a single peptide stably trapped at the constriction zone, we acknowledge

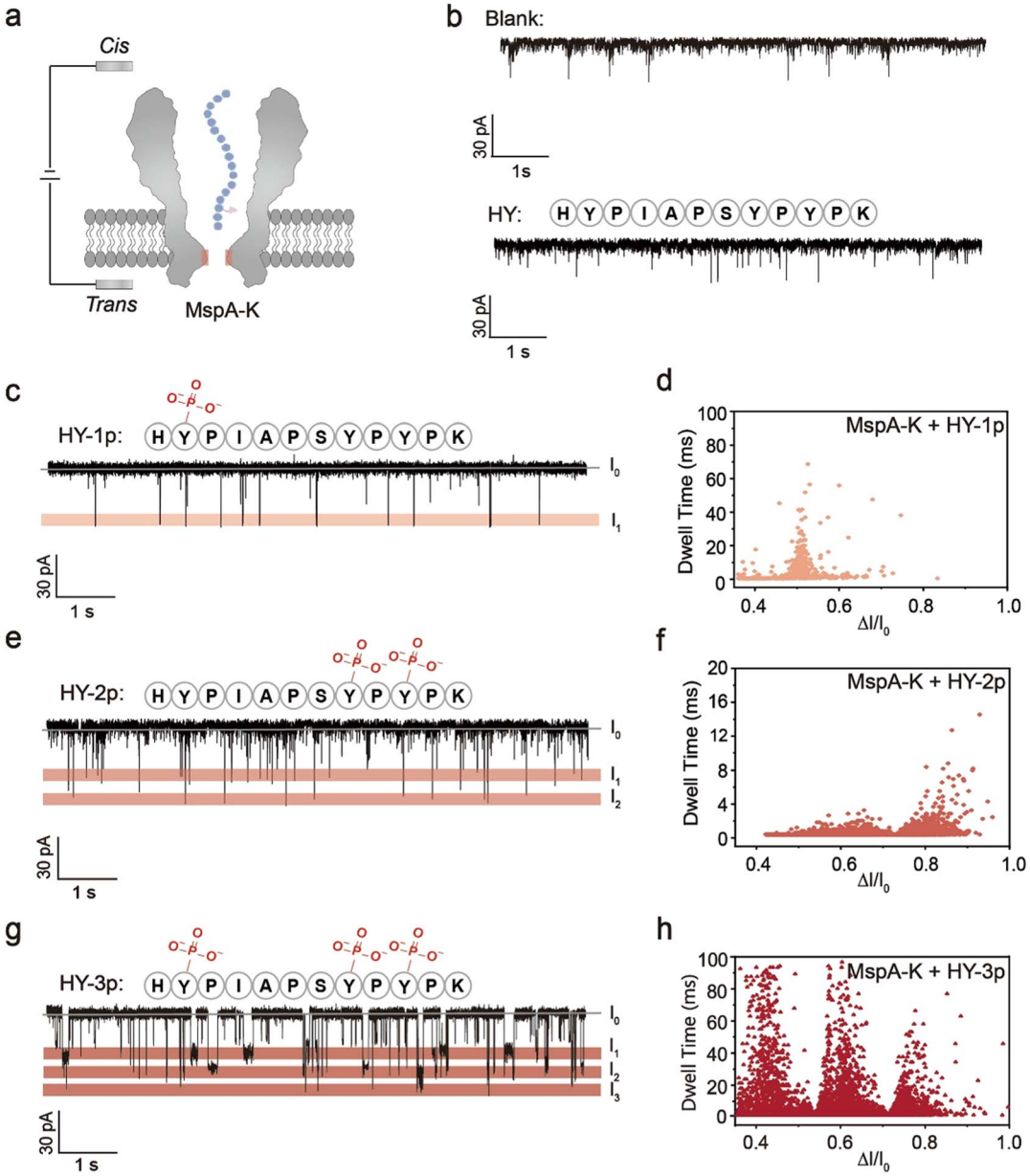

Fig. 3 (a) Schematic representation of MspA-K nanopore for the detection of phosphorylated peptides. (b) Representative current trace of MspA-K nanopore for blank and the unmodified peptide (HY). Representative current trace (c) and scatter-plot of $\Delta I/I_0$ (d) for HY-1p using the MspA-K nanopore. (e) and (f) Representative current trace and scatter-plot of $\Delta I/I_0$ for HY-2p using MspA-K. (g) and (h) Representative current trace and scatter-plot of $\Delta I/I_0$ for HY-3p using MspA-K. ΔI represents the change in current caused by the translocation of peptides through the nanopore, while I_0 refers to the open pore current. All data were acquired in the buffer of 1.0 M NaCl, 10 mM HEPES, pH 7.4.

that the actual nanopore translocation is a highly complex dynamic process. Mesoscopic phenomena such as voltage-driven polymer stretching,[42] local ion concentration polarization induced by multi-phosphate groups,[24] and occasional multiple peptide trapping likely play roles in the comprehensive experimental signals. A systematic and multiscale investigation of these dynamic conformational changes and electrokinetic effects will be the subject of our future research.

Recognition of PTM in real-world protein fragment

Building on these findings, we further investigated the potential of MspA nanopores carrying polar charged amino acids for detecting PTMs in real-world protein sequences modified by glycosylation, methylation, and acetylation. The results showed that the MspA-E nanopore effectively discriminated between non-glycosylated and mono-glycosylated sequences of the MUC1 protein (Fig. 5a and b). Similarly, the MspA-H nanopore successfully detected methylation modifications in histone-derived peptide sequences (Fig. 5c and d), while the MspA-K

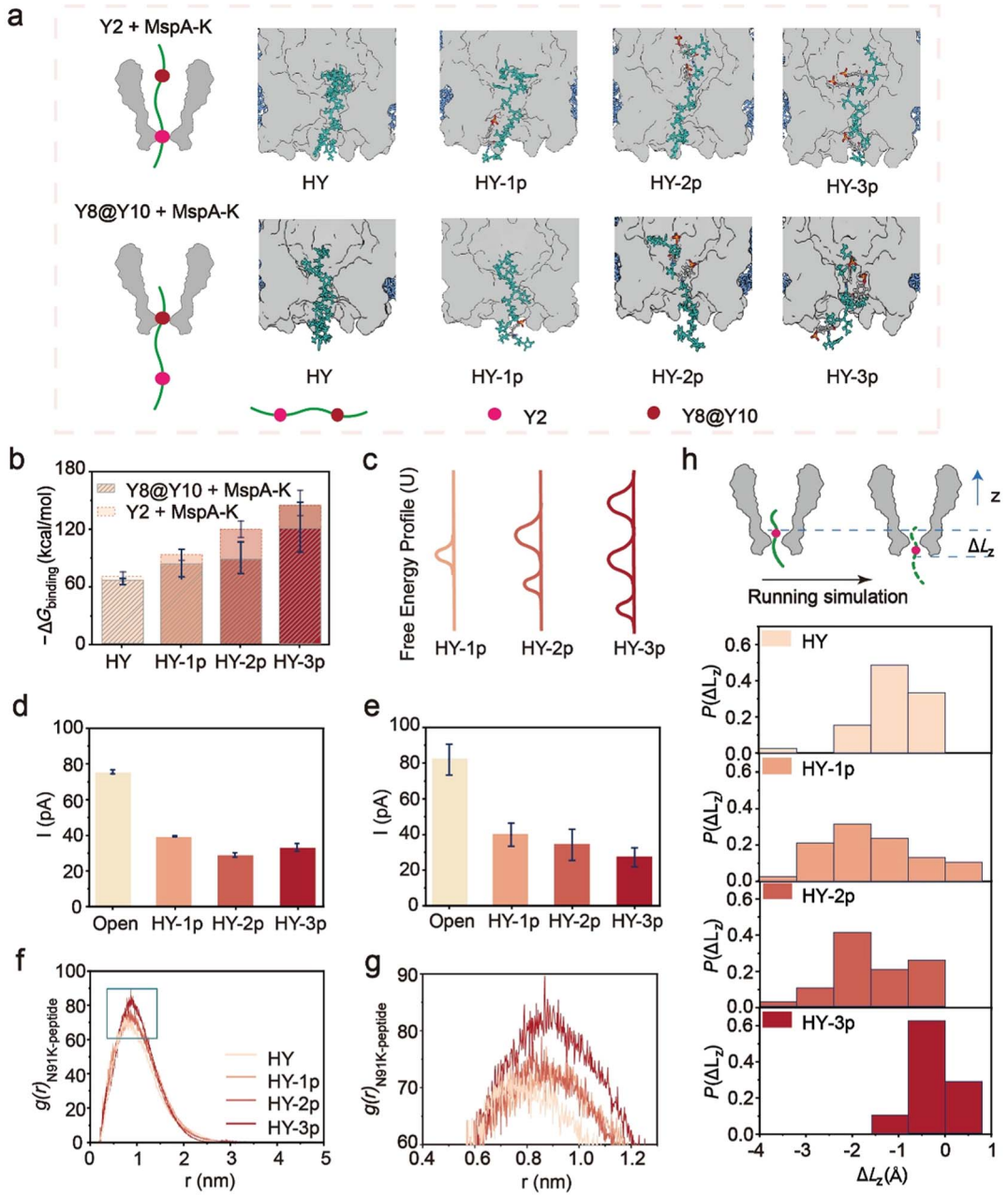

Fig. 4 (a) All-atom molecular dynamics simulations of phosphorylated peptides positioned near MspA-K at residues Y8@Y10 and Y2. (b) Binding free energy with MspA-K and the peptide. (c) Translocation energy barriers: one (HY-1p), two (HY-2p), and three (HY-3p). (d) Experimentally measured current blockade. (e) Simulated current blockade levels (Y8@Y10 + MspA-K). (f) The radial distribution function (RDF) of the interaction distance between K91 and peptides. (g) Enlarged view of the region indicated by the box in (f). (h) Probability distribution of peptides displacement under electric field driving during simulated observation time. HY-1p and HY-2p show broad displacement distributions with short translocation times, while HY-3p exhibits a narrower distribution and longer dwell time in the nanopore. ΔL_z is the center-of-mass displacement of the peptide. All simulated results represent the average of three independent parallel simulations.

nanopore demonstrated excellent recognition ability for an acetylated α-tubulin fragment (Fig. 5e and f).

This analysis revealed that MspA mutants carrying polar charged residues (*e.g.*, MspA-E, MspA-D, MspA-H, and MspA-K) exhibited significantly improved PTM recognition capabilities compared with other variants (Fig. S42–S49). Notably, initial experiments were performed in a buffer solution mimicking physiological conditions (pH 7.4), but the translocation frequency of the target peptide was very low. Therefore, buffers with adjusted pH values were subsequently used according to the isoelectric points of the peptides. Guided by these results, we next applied trypsin digestion to both MUC1 and eukaryotically expressed glycosylated MUC1, generating complex mixtures of peptide fragments (Fig. 5g). Based on the radar plot analysis, MspA-E and MspA-D were selected for detection of these digests. Representative current traces obtained using

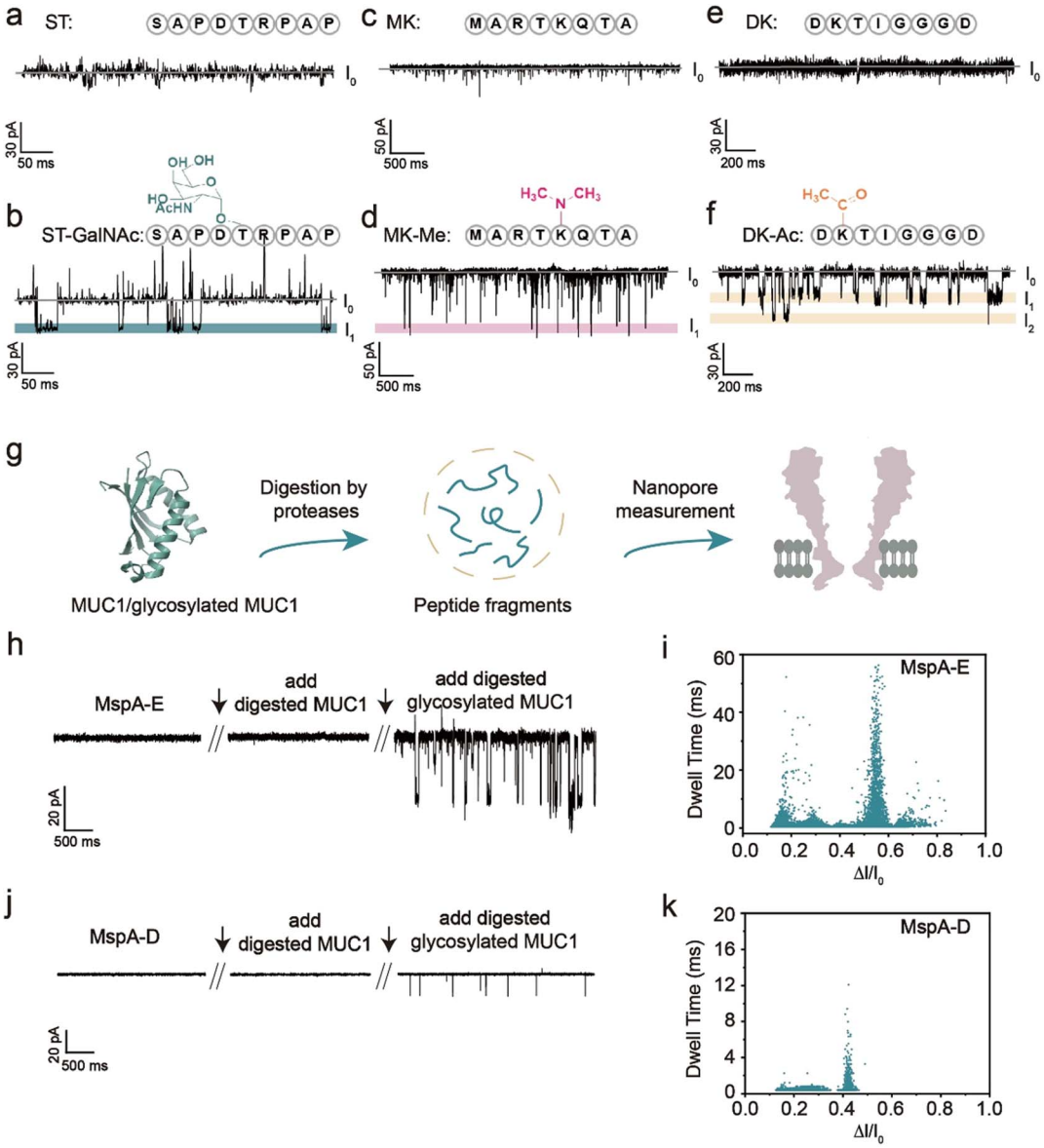

Fig. 5 Detection of PTM groups in real-world protein fragments using MspA mutants. (a and b) Representative current traces of ST/ST-GalNAc using the MspA-E nanopore. The $\Delta I/I_0$ of ST-GalNAc was 0.730 ± 0.003. The data were acquired in the buffer of 1.0 M NaCl, 10.0 mM HEPES, pH 9.0. (c and d) Representative current traces of MK/MK-Me using the MspA-H. The $\Delta I/I_0$ of MK-Me was 0.770 ± 0.001. The data were acquired in the buffer of 1.0 M NaCl, 10.0 mM HEPES, pH 12.0. (e and f) Representative current traces of DK/DK-Ac using the MspA-H. The $\Delta I/I_0$ of DK-Ac was 0.390 ± 0.004 and 0.820 ± 0.004. The data were acquired in the buffer of 1.0 M NaCl, 10.0 mM HEPES, pH 6.0. (g) Schematic illustration of the process involving tryptic digestion and nanopore detection of both MUC1 and glycosylated MUC1 protein. Representative current traces (h) and scatter plot (i) of trypsin-digested MUC1 and glycosylated MUC1 using the MspA-E nanopore. (j and k) Corresponding data obtained with the MspA-D nanopore.

MspA-E are shown in Fig. 5h, with the corresponding scatter plot and histogram of current blockage ratios ($\Delta I/I_0$) in Fig. 5i and S50.

The data revealed five distinct clusters. To interpret these clusters, we first characterized the expected digestion products of the MUC1 construct. Trypsin cleavage is restricted to three specific sites (Table S9) due to proline residues in KP/RP sequences, yielding three major peptide fragments. Each fragment contains multiple serine residues that can be *O*-glycosylated. Because the protein was expressed in mammalian cells, these serines may carry various mucin-type glycans, including αGalNAc, αNeu5Ac-(2,6)-αGalNAc, and βGal-(1,3)-αGalNAc.[43] Thus, the glycopeptides are highly heterogeneous. The five clusters do not directly represent five specific glycan structures; instead, they represent five populations of events resolvable under our conditions. To confirm their glycosylation origin, we analyzed unglycosylated MUC1 (prokaryotic expression) under identical conditions, which produced only one or two clusters (bare peptides). By comparison, the additional clusters in the mammalian sample were attributed to distinct glycosylation

states/types. Therefore, the five clusters reflect the heterogeneity of *O*-glycosylation that MspA-E can discriminate. In contrast, MspA-D nanopores resolved only three distinct clusters under the same conditions (Fig. 5j–k and S51). We further extended this strategy to Tau and phosphorylated Tau proteins (Figure S52). Remarkably, MspA-E resolved three additional current clusters specifically associated with phosphorylated Tau samples. These results not only highlight the pivotal role of polar charged residues in PTM recognition within nanopores, but also provide strong experimental support for the development of multiplex PTM detection platforms using MspA nanopores.

Conclusions

In summary, we systematically demonstrate the critical role of rationally engineered MspA nanopores in advancing the detection and analysis of post-translational modifications (PTMs). By introducing polar and charged amino acid residues into specific constriction sites, we markedly enhanced the nanopore's ability to selectively recognize diverse PTMs. However, the underlying mechanism is not reducible to simple electrostatic or hydrogen-bonding interactions alone. Instead, our data indicate that the enhanced sensitivity and selectivity arise from a complex interplay of multiple physical effects, including electrostatic forces, EOF, local ion concentration polarization induced by the PTM itself, and peptide backbone stretching dynamics. This structural optimization enabled high-resolution single-molecule detection across a broad spectrum of PTMs, including phosphorylation, acetylation and glycosylation, allowing both qualitative identification and quantitative differentiation. Notably, the engineered nanopores exhibited the capacity to discriminate phosphorylation stoichiometry, a long-standing challenge for conventional analytical methods. These findings underscore the importance of integrating multiple nanoscale interactions.

Our work establishes a robust framework for the functional design and optimization of biological nanopores. Incorporating polar and charged residues into the constriction region, while also considering the resultant electroosmotic and polarization effects, significantly broadens the spectrum of detectable PTMs and expands the utility of nanopore sensing for complex proteomic analysis. This strategy offers new technical pathways for high-throughput, multiplexed, and label-free PTM profiling, paving the way for real-time monitoring in systems biology, disease biomarker discovery, and clinical diagnostics. With continued advances in nanopore engineering, we anticipate that such tailored nanopores will become very useful tools for proteomic research and translational applications.

Author contributions

X. L., H. W. and F. X. supervised the project. X. L., S. L., H. W. and F. X. conceived and designed the study. S. L. designed and synthesized the protein. S.L. and Y. Y. analyzed the data and prepared figures. S. L. and Y. L. assisted with experiments. M. L. conducted molecular dynamics simulations. S. L., X. L., H. W. and F. X. drafted the manuscript. S. L., Y. Y., X. L., H. W. and F. X. revised the manuscript. All authors contributed to the writing of the manuscript.

Conflicts of interest

There are no conflicts to declare.

Data availability

The data supporting this article have been included as part of the supplementary information (SI). Supplementary information: detailed synthetic, experimental procedures, instrumentation, materials, supporting data. Part of the raw data are additionally available at Figshare with DOI: https://doi.org/10.6084/m9.figshare.30383926. See DOI: https://doi.org/10.1039/d6sc01451h.

Acknowledgements

This work was supported by the National Natural Science Foundation of China (22474131, U24A20502), the National Key R&D Program of China (2021YFA1200403 and 2025YFC2708401), the Natural Science Foundation of Hubei Province (2024AFA001), the Natural Science Foundation of Shenzhen (JCYJ20230807113706013).

Notes and references

1 M. Mann and O. N. Jensen, *Nat. Biotechnol.*, 2003, **21**, 255–261.
2 M. J. Suskiewicz, *BioEssays*, 2024, **46**, 2300178.
3 Q. Zhong, X. Xiao, Y. Qiu, Z. Xu, C. Chen, B. Chong, X. Zhao, S. Hai, S. Li, Z. An and L. Dai, *MedComm*, 2023, **4**, e261.
4 A. C. Conibear, *Nat. Rev. Chem.*, 2020, **4**, 674–695.
5 J. M. Lee, H. M. Hammarén, M. M. Savitski and S. H. Baek, *Nat. Commun.*, 2023, **14**, 201.
6 Y. Chen and Y. Wang, *Trends Biochem.*, 2022, **47**, 189–193.
7 A. S. Venne, L. Kollipara and R. P. Zahedi, *Proteomics*, 2014, **14**, 513–524.
8 Y. L. Deribe, T. Pawson and I. Dikic, *Nat. Struct. Mol. Biol.*, 2010, **17**, 666–672.
9 X. Cui, J. Wang, K. Li, B. Lv, B. Hou and Z. Ding, *J. Genet. Genomics*, 2024, **51**, 279–291.
10 J. Hermann, L. Schurgers and V. Jankowski, *Mol. Aspects Med.*, 2022, **86**, 101066.
11 J. V. Torres-Perez, J. Irfan, M. R. Febrianto, S. Di Giovanni and I. Nagy, *Trends Pharmacol. Sci.*, 2021, **42**, 897–911.
12 Y. Wang, J. Zhang, B. Li and Q.-Y. He, *Small Methods*, 2019, **3**, 1900041.
13 S. Doll and A. L. Burlingame, *ACS Chem. Biol.*, 2015, **10**, 63–71.
14 T. Liu, W. Zhang, Z. Zhang, M. Chen, J. Wang, X. Qian and W. Qin, *Anal. Chem.*, 2018, **90**, 2186–2192.
15 D. Virág, B. Dalmadi-Kiss, K. Vékey, L. Drahos, I. Klebovich, I. Antal and K. Ludányi, *Chromatographia*, 2020, **83**, 1–10.

16 L. Restrepo-Pérez, C. H. Wong, G. Maglia, C. Dekker and C. Joo, *Nano Lett.*, 2019, **19**, 7957–7964.
17 L. Restrepo-Pérez, C. Joo and C. Dekker, *Nat. Nanotechnol.*, 2018, **13**, 786–796.
18 T. Hattori and S. Koide, *Curr. Opin. Struct. Biol.*, 2018, **51**, 141–148.
19 C. Solier and H. Langen, *Proteomics*, 2014, **14**, 774–783.
20 Y. Wu and J. J. Gooding, *Chem. Soc. Rev.*, 2022, **51**, 3862–3885.
21 J. J. Kasianowicz, E. Brandin, D. Branton and D. W. Deamer, *Proc. Natl. Acad. Sci. U. S. A*, 1996, **93**, 13770–13773.
22 C. Cao, P. Magalhães, L. F. Krapp, J. F. Bada Juarez, S. F. Mayer, V. Rukes, A. Chiki, H. A. Lashuel and M. Dal Peraro, *ACS Nano*, 2024, **18**, 1504–1515.
23 X. Zhao, H. Qin, M. Tang, X. Zhang and G. Qing, *Trac. Trends Anal. Chem.*, 2024, **173**, 117658.
24 X. Chen, J. W. van de Sande, J. Ritmejeris, C. Wen, H. Brinkerhoff, A. H. Laszlo, B. Albada and C. Dekker, *ACS Nano*, 2024, **18**, 28999–29007.
25 A. Singh, *Nat. Methods*, 2023, **20**, 1130.
26 M. Zhang, C. Tang, Z. Wang, S. Chen, D. Zhang, K. Li, K. Sun, C. Zhao, Y. Wang, M. Xu, L. Dai, G. Lu, H. Shi, H. Ren, L. Chen and J. Geng, *Nat. Methods*, 2024, **21**, 609–618.
27 H. Niu, M.-Y. Li, Y. Gao, J.-G. Li, J. Jiang, Y.-L. Ying and Y.-T. Long, *Nat. Chem. Biol.*, 2025, **21**, 716–726.
28 T. Ensslen, K. Sarthak, A. Aksimentiev and J. C. Behrends, *J. Am. Chem. Soc.*, 2022, **144**, 16060–16068.
29 Z. Li, Y. Yi, Y. Zhang, Y. Xiao, Q. Ren, K. Zhou, L. Liu and H.-C. Wu, *Angew. Chem., Int. Ed.*, 2025, **64**, e202423801.
30 N. Kitamura and J. J. Galligan, *Biochem. J.*, 2023, **480**, 1241–1265.
31 R. Bischoff and H. Schlüter, *Proteomics*, 2012, **75**, 2275–2296.
32 F.-N. Meng, Y.-L. Ying, J. Yang and Y.-T. Long, *Anal. Chem.*, 2019, **91**, 9910–9915.
33 X. Li, Y. Wang, S. Zhang, P. Zhang and S. Huang, *ACS Sens.*, 2024, **9**, 1359–1371.
34 J. Zhang, Y. Wang, Y. Wang, P. Zhang, H.-Y. Chen and S. Huang, *Nano Lett.*, 2022, **22**, 5561–5569.
35 S. Yan, J. Zhang, Y. Wang, W. Guo, S. Zhang, Y. Liu, J. Cao, Y. Wang, L. Wang, F. Ma, P. Zhang, H.-Y. Chen and S. Huang, *Nano Lett.*, 2021, **21**, 6703–6710.
36 S. F. Mayer, M. F. Mitsioni, P. Robin, L. van den Heuvel, N. Ronceray, M. J. Marcaida, L. A. Abriata, L. F. Krapp, J. S. Anton, S. Soussou, J. Jeanneret-Grosjean, A. Fulciniti, A. Möller, S. Vacle, L. Feletti, H. Brinkerhoff, A. H. Laszlo, J. H. Gundlach, T. Emmerich, M. Dal Peraro and A. Radenovic, *Nat. Nanotechnol.*, 2026, **21**, 116–124.
37 L. Harrington, L. T. Alexander, S. Knapp and H. Bayley, *ACS Nano*, 2019, **13**, 633–641.
38 W.-H. Lan, H. He, H. Bayley and Y. Qing, *J. Am. Chem. Soc.*, 2024, **146**, 24265–24270.
39 Y.-L. Ying, J. Yang, F.-N. Meng, S. Li, M.-Y. Li and Y.-T. Long, *Research*, 2019, **2019**, 8.
40 S. Li, X.-Y. Wu, M.-Y. Li, S.-C. Liu, Y.-L. Ying and Y.-T. Long, *Small Methods*, 2020, **4**, 2000014.
41 C. B. Rosen, D. Rodriguez-Larrea and H. Bayley, *Nat. Biotechnol.*, 2014, **32**, 179–181.
42 I. C. Nova, J. Ritmejeris, H. Brinkerhoff, T. J. R. Koenig, J. H. Gundlach and C. Dekker, *Nat. Biotechnol.*, 2024, **42**, 710–714.
43 V. Lakshminarayanan, P. Thompson, M. A. Wolfert, T. Buskas, J. M. Bradley, L. B. Pathangey, C. S. Madsen, P. A. Cohen, S. J. Gendler and G.-J. Boons, *Proc. Natl. Acad. Sci. U. S. A.*, 2012, **109**, 261–266.